Two new double-lined spectroscopic binary white dwarfs

Mukremin Kilic [1]★ A. Bédard,[2] P. Bergeron[2] and Alekzander Kosakowski[1]

[1]*Homer L. Dodge Department of Physics and Astronomy, University of Oklahoma, 440 W. Brooks St, Norman, OK 73019, USA*
[2]*Département de Physique, Université de Montréal, C.P. 6128, Succ. Centre-Ville, Montréal, QC H3C 3J7, Canada*

ABSTRACT

We present radial velocity observations of four binary white dwarf candidates identified through their overluminosity. We identify two new double-lined spectroscopic binary systems, WD 0311–649 and WD 1606+422, and constrain their orbital parameters. WD 0311–649 is a 17.7 h period system with a mass ratio of 1.44 ± 0.06 and WD 1606+422 is a 20.1 h period system with a mass ratio of 1.33 ± 0.03. An additional object, WD 1447–190, is a 43 h period single-lined white dwarf binary, whereas WD 1418–088 does not show any significant velocity variations over time-scales ranging from minutes to decades. We present an overview of the 14 overluminous white dwarfs that were identified by Bédard et al., and find the fraction of double- and single-lined systems to be both 31 per cent. However, an additional 31 per cent of these overluminous white dwarfs do not show any significant radial velocity variations. We demonstrate that these must be in long-period binaries that may be resolved by *Gaia* astrometry. We also discuss the overabundance of single low-mass white dwarfs identified in the SPY survey, and suggest that some of those systems are also likely long-period binary systems of more massive white dwarfs.

Key words: stars: evolution – stars: individual: WD 0311–649, WD 1418–088, WD 1447–190, WD 1606+422 – white dwarfs.

1 INTRODUCTION

Double white dwarfs with well-measured orbital and physical parameters provide essential constraints on binary population synthesis models and the stability of mass transfer in their progenitor systems. However, the number of double white dwarfs with well-measured primary and secondary masses and orbital parameters is rather small, with only 8 eclipsing and 17 double-lined (SB2) spectroscopic binaries currently known.

The eclipsing systems are dominated by extremely low-mass (ELM; $M \sim 0.2\,M_\odot$) white dwarfs (e.g. Steinfadt et al. 2010; Brown et al. 2011, 2017; Burdge et al. 2019). This is not surprising, as the eclipse searches are most sensitive to short-period systems, and the formation of ELM white dwarfs requires close binary companions (Li et al. 2019). ELM white dwarfs tend to have relatively massive companions (Andrews, Price-Whelan & Agüeros 2014; Boffin 2015; Brown, et al. 2016), and six of the known eclipsing systems have relatively large mass ratios. The two exceptions are the low-mass white dwarfs CSS 41177 ($0.38+0.32\,M_\odot$; Bours et al. 2014) and J1152+0248 ($0.47+0.44\,M_\odot$; Hallakoun et al. 2016).

Double-lined spectroscopic binaries, on the other hand, are biased towards equal-brightness and equal-mass systems. The first SB2 white dwarf system, L870–2, was identified as a potential binary

based on its overluminosity compared to other white dwarfs, and was confirmed to be a double-lined spectroscopic binary by Saffer, Liebert & Olszewski (1988). Radial velocity surveys in the late 1990s and early 2000s, mainly the ESO supernovae type Ia progenitor survey (SPY; Napiwotzki et al. 2001), increased the number of SB2 systems to 13 (Marsh 1995; Moran, Marsh & Bragaglia 1997; Maxted, Marsh & Moran 2002; Napiwotzki, et al. 2002; Karl, et al. 2003; Napiwotzki, et al. 2007). With the serendipitous discovery of an additional system by Debes et al. (2015), and three more by Rebassa-Mansergas et al. (2017), the total number of double-lined WDs with well-measured orbital parameters and mass ratios is now 17. There are nine more SB2 systems identified by Napiwotzki et al. (2019) that need follow-up radial velocity observations for orbital constraints.

Recently, Bédard, Bergeron & Fontaine (2017) performed a spectroscopic and photometric analysis of 219 white dwarfs with trigonometric parallax measurements available at the time, and identified 15 unresolved double-degenerate binary candidates, including several previously known double-lined spectroscopic binaries. Bergeron et al. (2019) presented an updated analysis of these objects based on *Gaia* Data Release 2 parallaxes, and confirmed the overluminous nature of all but one of these targets, WD1130+189. Here we present follow-up spectroscopy of four of these white dwarfs, three of which are confirmed to be binary systems. We present an overview of the overluminous white dwarf sample from Bédard et al. (2017) and discuss the period and mass distribution of
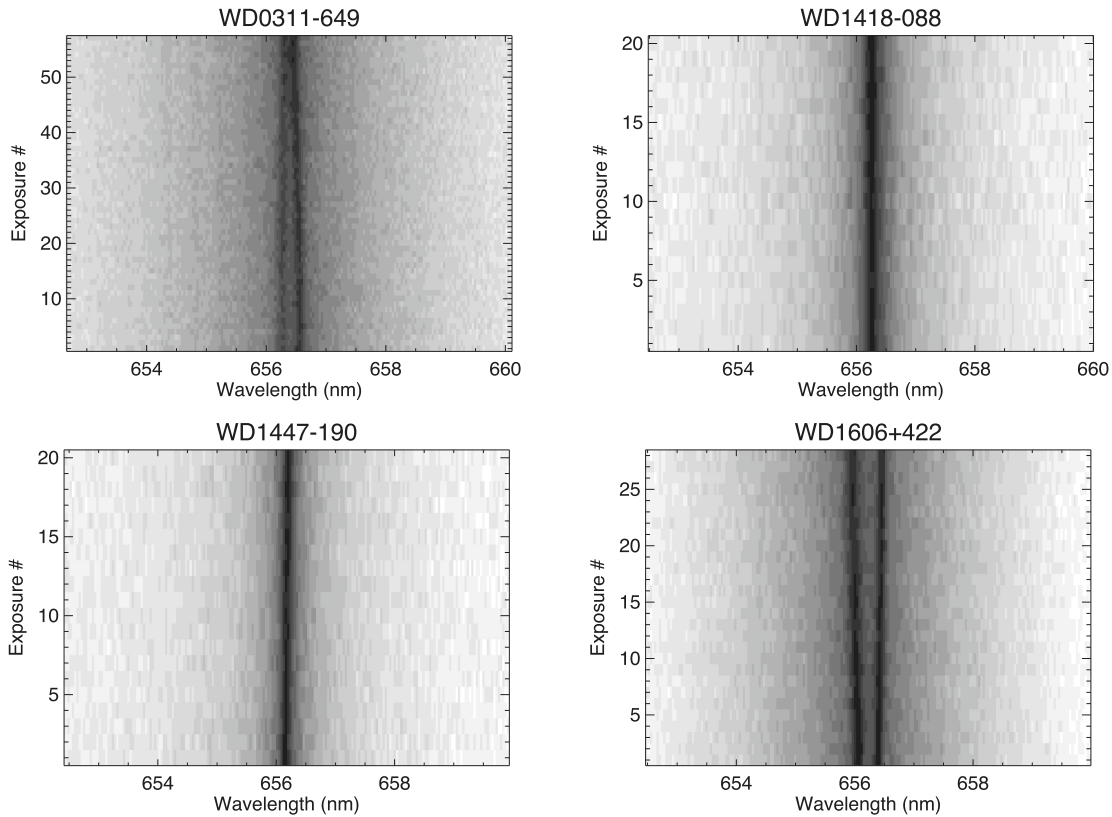
★ E-mail: kilic@ou.edu

Figure 1. Gemini time-resolved spectroscopy of four white dwarfs with back-to-back exposures. WD 0311−649 and WD 1606+422 turn out to be double-lined spectroscopic binaries, whereas WD 1447−190 is a single-lined binary. The remaining target, WD 1418−088, does not show any significant radial velocity variability.

the sample, as well as the fractions of SB2, SB1, and systems that show no significant radial velocity variability.

2 OBSERVATIONS

We used the High Resolution Echelle Spectrometer (HIRES, Vogt et al. 1994) on the Keck I telescope at Mauna Kea Observatory in Hawaii to observe three of our targets on UT 2018 June 18. Unfortunately, our three half-night long observing run was limited to a period of about only 2 h due to volcanic activity and vog. We used the blue cross disperser with a 1.15 arcsec slit resulting in a spectral resolution of 37 000. We used the MAuna Kea Echelle Extraction (MAKEE) package to analyse the HIRES data.

We obtained follow-up optical spectroscopy of all four of our targets using the 8 m Gemini telescopes equipped with the Gemini Multi-Object Spectrograph (GMOS) as part of the queue programmes GN-2018A-Q-116 and GS-2018B-Q-117. We used the R831 grating and a 0.25 arcsec slit, providing wavelength coverage from 5380 to 7740 Å and a resolution of 0.376 Å per pixel. Each spectrum has a comparison lamp exposure taken within 10 min of the observation time. We used the IRAF GMOS package to reduce these data.

Our initial observing strategy included a series of back-to-back exposures to look for short-period systems. Fig. 1 shows the Gemini/GMOS trailed spectra for all four targets based on these back-to-back exposures. We obtained 57 × 150 s exposures of WD 0311−649 on UT 2018 October 2, 20 × 300 s exposures of WD 1418−088 on UT 2018 July 1, 20 × 300 s exposures of WD 1447−190 on UT 2018 July 10, and 28 × 245 s exposures of WD 1606+422 on

UT 2018 September 11. This figure reveals two double-lined binary systems, WD 0311−649 and WD 1606+422, where the double Hα lines are seen converging and diverging over a few hours, respectively. One of the single-lined objects, WD 1447−190, also showed significant velocity shifts in the back-to-back exposures, but the other, WD 1418−088, did not show any significant variations over a period of 1.8 h, and we decided not to follow it up further (see more below). To constrain the orbital parameters of the three velocity variable systems, we obtained additional spectroscopy with different nightly cadences as part of the Gemini Fast Turnaround and queue programmes GN-2019A-FT-208, GS-2019A-FT-202, and GS-2019B-Q-113.

We obtained seven additional spectra of WD 1447−190 on UT 2019 March 1–3 at the 4.1 m SOAR telescope equipped with the Goodman High Throughput spectrograph (Clemens, Crain & Anderson 2004) with the 930 line mm^{-1} grating and the 1.03 arcsec slit. This set-up provides 2.2 Å spectral resolution over the range 3550–5250 Å. The SOAR spectra were obtained as part of the NOAO programme 2019A-0134.

3 RADIAL VELOCITY MEASUREMENTS

We use the core of the Hα line to measure the radial velocities of our single- and double-lined systems. After normalizing the continuum, we use a quadratic polynomial plus a Lorentzian or Voigt profile to fit the line wings and the line cores, respectively. We find the best-fitting parameters with LMFIT, a version of the Levenberg–Marquardt algorithm adapted for PYTHON (Newville et al. 2014). We apply the standard Solar system barycentric corrections, and use the night skylines to check the spectrograph flexure.
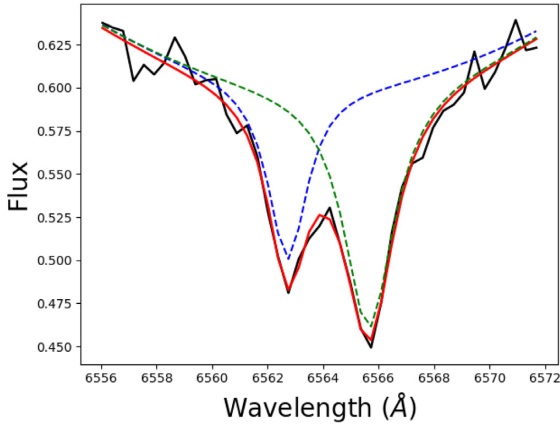
Figure 2. Best-fitting Lorentzian profiles to the Hα line cores visible in the double-lined spectroscopic binary WD 0311–649 (blue and green dotted lines). The red solid line shows the composite best-fitting model.

Fig. 2 shows the best fit to the first Gemini exposure on the double-lined system WD 0311–649, demonstrating our procedure. Here the dotted blue and green lines show the best-fitting Lorentzian profiles to the two Hα line cores, and the red line shows the composite best-fitting model. The formal measurement errors on the two Hα line centres in this spectrum are 0.06 and 0.05 Å, respectively. Napiwotzki et al. (2019) demonstrated that formal fitting errors tend to be underestimated, and that error estimates based on bootstrapping are better for including uncertainties from imperfections of the input data and non-Gaussian noise. We use a similar bootstrapping procedure, and randomly select N points of the observed spectra, where points can be selected more than once. We use the bootstrapped spectra to rederive velocities, repeating this procedure 1000 times. We add the standard deviation of the velocity measurements from the bootstrapped spectra and the formal fitting errors in quadrature to estimate the total errors in each velocity measurement. This procedure gives 4 km s^{-1} errors for both lines in the spectrum shown in Fig. 2.

4 ATMOSPHERIC PARAMETER DETERMINATION

Bédard et al. (2017) showed that it is possible to constrain the atmospheric parameters ($T_{\rm eff}$ and log g) of both white dwarfs in an unresolved DA+DA binary system by combining spectroscopic, photometric, and astrometric information. More specifically, they developed a deconvolution procedure that involves fitting simultaneously the observed Balmer lines and spectral energy distribution with composite model atmospheres. We briefly describe this method here, as we apply it in Section 5 to revisit the atmospheric properties of our four binary candidates in light of our new data.

The radiative flux f_ν received at the Earth from an unresolved double-degenerate system is simply the sum of the Eddington fluxes emitted by the individual components, properly weighted by their respective solid angle:

$$f_\nu = 4\pi \left(\frac{R_1}{D}\right)^2 H_{\nu,1} + 4\pi \left(\frac{R_2}{D}\right)^2 H_{\nu,2} . \quad (1)$$

Assuming that the distance D is known from a trigonometric parallax measurement, the right-hand side of this equation depends only on the four atmospheric parameters $T_{\rm eff, 1}$, log g_1, $T_{\rm eff, 2}$, and log g_2. Indeed, for given values of these quantities, the Eddington

fluxes $H_{\nu, 1}$ and $H_{\nu, 2}$ are obtained from model atmospheres, and the radii R_1 and R_2 are obtained from evolutionary sequences. In what follows, we use pure-hydrogen model atmospheres similar to those described in Tremblay & Bergeron (2009) together with 3D hydrodynamical corrections from Tremblay et al. (2013), as well as evolutionary models similar to those described in Fontaine, Brassard & Bergeron (2001) with carbon/oxygen cores ($X_{\rm C} = X_{\rm O} = 0.5$) and standard 'thick' hydrogen layers ($M_{\rm H}/M_\star = 10^{-4}$).

Both our spectroscopic and photometric analyses are based on equation (1). In the spectroscopic case, the observed optical spectrum (left-hand side) is compared to a weighted sum of two synthetic spectra (right-hand side). Since only the shape of the Balmer lines is of interest, the observed and (combined) synthetic spectra are normalized to a continuum set to unity before the comparison is carried out. In the photometric case, a set of average fluxes measured in some optical and infrared bandpasses (left-hand side) is compared to a weighted sum of two synthetic spectra properly averaged over the corresponding bandpass filters (right-hand side). We adopt the zero-points given in Holberg & Bergeron (2006) to convert observed magnitudes into average fluxes, and neglect reddening since all of our systems are within 50 pc (see Table 1). Note that absolute fluxes are required here since we are interested in the overall energy distribution.

Our fitting procedure uses the Levenberg–Marquardt algorithm to find the values of $T_{\rm eff, 1}$, log g_1, $T_{\rm eff, 2}$, and log g_2 that minimize the difference between the two sides of the equation for both the spectroscopic and photometric observations simultaneously. We stress that such a unified approach is mandatory to achieve reliable results, especially when all four atmospheric parameters are allowed to vary. We do not fit for distance, since distances are precisely determined by *Gaia* DR2 (Gaia Collaboration 2018) for all four targets (Table 1).

In our analysis reported below, we employ the same spectroscopic and photometric data as in Bédard et al. (2017), with the exceptions that we make use of our new SOAR spectrum for WD 1447–190, and that we add the Pan-STARRS *grizy* magnitudes (Chambers et al. 2016) to our photometric fits for WD 1418–088, WD 1447–190, and WD 1606+422.

5 RESULTS

5.1 WD 0311–649

Fig. 3 shows the radial velocity measurements and the Lomb–Scargle periodogram for the double-lined spectroscopic binary WD 0311–649. We use the IDL program MPRVFIT (De Lee et al. 2013) in the SB2 mode to find the best-fitting orbit. Excluding the three spectra where the Hα lines from both stars overlap and appear as a single line, we have 68 radial velocity measurements for each star. The best-fitting orbital parameters and their formal errors are $P = 0.739\,57 \pm 0.000\,01$ d, $K_1 = 86.5 \pm 1.7$ km s^{-1}, $K_2 = 60.0 \pm 2.1$ km s^{-1}, $\gamma_1 = 48.7 \pm 1.7$ km s^{-1}, and a velocity offset of $\gamma_2 - \gamma_1 = 11.1 \pm 2.7$ km s^{-1}.

The Lomb–Scargle diagram shows that there are significant aliases, which are offset from each other by multiples of 0.001 35 d. Period aliases are the largest source of uncertainty in our orbital solutions. To constrain the impact of these aliases on our orbital solutions, we use a Monte Carlo approach, re-sampling the radial velocities with their errors and re-fitting orbital parameters 1000 times. This approach samples χ^2 space in a self-consistent way. We report the median value and errors derived from the 15.9 and 84.1 percentiles of the distributions for each orbital

Table 1. Orbital and physical parameters of the confirmed binary systems in the Bédard et al. (2017) sample of overluminous white dwarfs.

Object	ϖ (mas)	P (days)	Masses (M$_\odot$)	Type	Reference
WD0135–052	79.21 ± 0.04	1.56	0.47+0.52	SB2	Saffer et al. (1988)
WD0311–649	27.29 ± 0.03	0.74	0.39+0.55	SB2	This paper
WD1242–105	24.80 ± 0.04	0.12	0.39+0.56	SB2	Debes et al. (2015), Subasavage et al. (2017)
WD1606+422	23.07 ± 0.03	0.84	0.45+0.59	SB2	This paper
WD0101+048	44.86 ± 0.12	∼6.4 or 1.2	0.49+?	SB1	Maxted et al. (2000)
WD0326–273	43.43 ± 0.04	1.88	0.51+≥0.59	SB1	Nelemans et al. (2005)
WD1447–190	20.52 ± 0.05	1.79	0.41+0.33	SB1	This paper
WD1824+040	22.42 ± 0.09	6.27	0.43+≥0.52	SB1	Morales-Rueda et al. (2005)
WD1639+153	31.48 ± 0.11	4 yr	0.93 + 0.91 (DA+DA?)	Astrometric	Harris et al. (2013)
			0.98 + 0.69 (DA+DC?)		Harris et al. (2013)
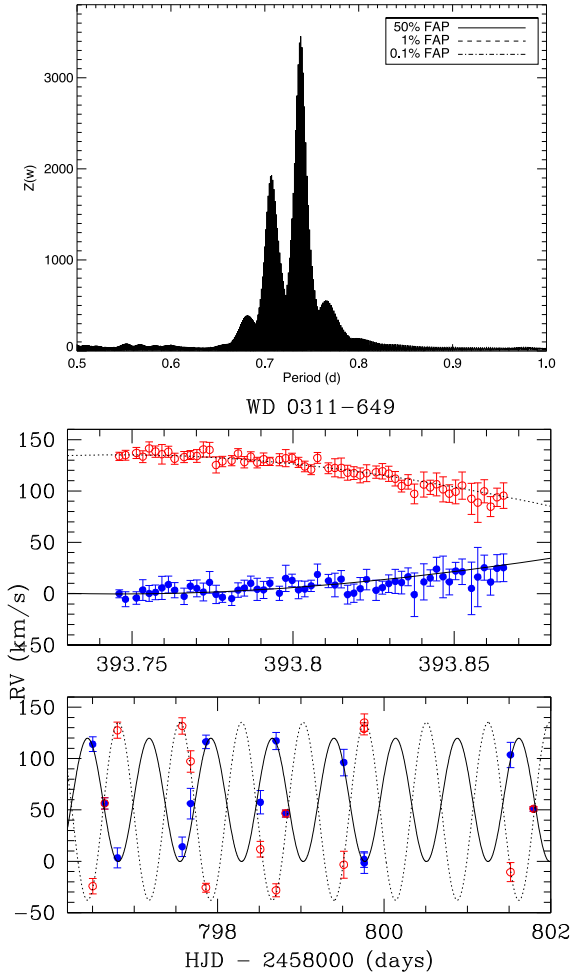
Figure 3. *Top:* Lomb–Scargle periodogram for WD 0311–649. *Middle and Bottom:* Radial velocity measurements (open and filled points) and the best-fitting orbital solutions (dotted and solid lines) for the two stars in WD 0311–649 assuming a circular orbit.

element. The best-fitting orbital parameters from the Monte Carlo simulations are $P = 0.739\,56^{+0.001\,34}_{-0.002\,67}$ d, $K_1 = 86.5^{+2.0}_{-1.7}$ km s^{-1}, $K_2 = 60.1^{+2.0}_{-2.1}$ km s^{-1}, $\gamma_1 = 48.4 \pm 1.7$ km s^{-1}, $\gamma_2 - \gamma_1 = 11.6^{+2.6}_{-2.7}$ km s^{-1}, and $\frac{K_1}{K_2} = 1.44 \pm 0.06$. These values are consistent with the formal estimates from MPRVFIT within the errors, though the error in period is significantly larger than the formal errors due to the aliasing present.

The individual masses of the two components can be derived from the orbital parameters. Since the difference in systemic velocities is equal to the difference in gravitational redshifts, we have

$$\gamma_2 - \gamma_1 = \frac{G}{c}\left(\frac{M_2}{R_2(M_2)} - \frac{M_1}{R_1(M_1)}\right)$$

$$= \frac{G}{c}\left(\frac{K_1 M_1/K_2}{R_2(K_1 M_1/K_2)} - \frac{M_1}{R_1(M_1)}\right), \qquad (2)$$

where $R(M)$ is the mass–radius relation obtained from our evolutionary sequences. For given values of $\gamma_2 - \gamma_1$ and K_1/K_2, this equation can be solved numerically for M_1 (and hence M_2). We find $M_1 = 0.385^{+0.060}_{-0.063}$ M$_\odot$ and $M_2 = 0.554^{+0.073}_{-0.082}$ M$_\odot$.

Fig. 4 displays our best model-atmosphere fit to the Balmer lines and the spectral energy distribution of WD 0311–649. In the minimization procedure, the surface gravities are held fixed to the values derived from the orbital solution, $\log g_1 = 7.55^{+0.14}_{-0.17}$ and $\log g_2 = 7.91^{+0.12}_{-0.16}$, so only the effective temperatures are treated as free parameters. Our fitting method yields $T_{\text{eff},1} = 12\,600 \pm 500$ K and $T_{\text{eff},2} = 12\,300 \pm 500$ K. Both the spectroscopic and photometric data are nicely reproduced by our composite model.

To validate our solution further, we compare in Fig. 5 the observed and predicted Hα features of WD 0311–649. Five of our Gemini spectra are co-added in order to increase the signal-to-noise ratio, and a wavelength shift is applied to the individual synthetic spectra to match the observed shift between the two line cores. The agreement is almost perfect, even though no fit was performed here, and thus confirms the accuracy of our atmospheric parameters. Finally, it is interesting that our solution places the secondary star within the ZZ Ceti instability strip, close to the blue edge (Gianninas, Bergeron & Ruiz 2011). Therefore, this object should be monitored for pulsations, which might, however, be difficult to detect due to the light of the primary star.

5.2 WD 1418–088

Fig. 6 shows the radial velocity measurements for WD 1418–088 from the SPY survey (top panel; Napiwotzki et al. 2019) and our Keck (middle panel) and Gemini (bottom panel) observations. WD 1418–088 does not show any significant radial velocity variations. We use the weighted mean velocity to calculate the χ^2 statistic for a constant velocity model. The probability, p, of obtaining the observed value of χ^2 or higher from random fluctuations of a constant velocity, taking into account the appropriate number of degrees of freedom, is 0.22. Hence, the null hypothesis cannot be rejected; the radial velocity measurements for WD 1418–088 are consistent with a constant velocity.
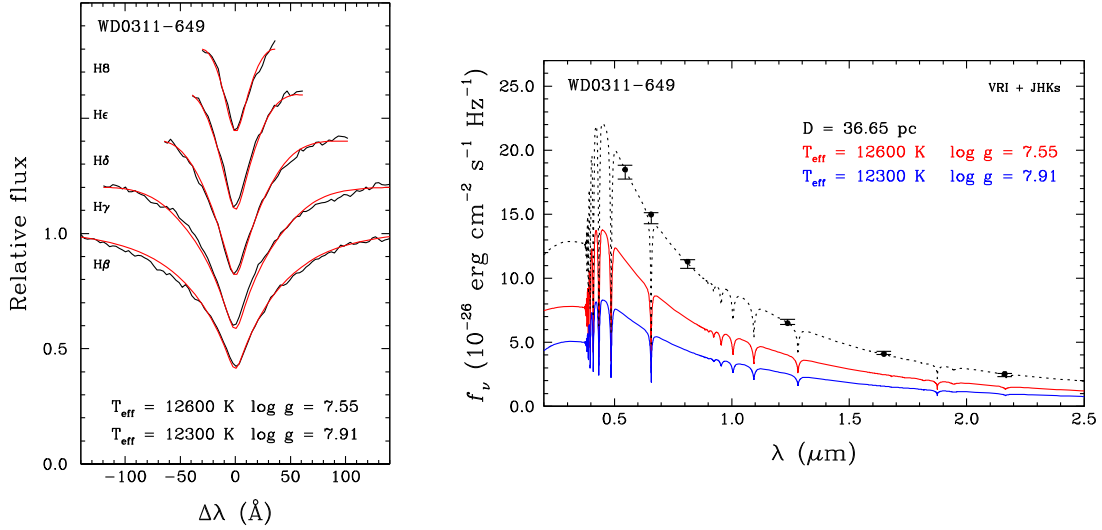
Figure 4. Best model-atmosphere fit to the Balmer lines (left-hand panel) and the spectral energy distribution (right-hand panel) of WD 0311–649. In the left-hand panel, the observed and synthetic spectra are displayed as the black and red lines, respectively. In the right-hand panel, the observed and synthetic average fluxes are shown as the error bars and filled circles, respectively; in addition, the red and blue lines show the contribution of each component to the total monochromatic model flux, which is displayed as the black dotted line. The best-fitting atmospheric parameters are given in both the panels.
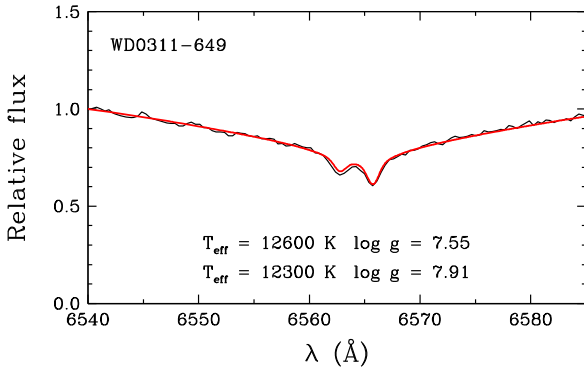

Figure 5. Comparison of the observed double H α feature of WD 0311–649, shown as the black line, with that predicted by our best model-atmosphere fit, displayed as the red line.

Figure 6. VLT (top), Keck (middle), and Gemini (bottom) radial velocity observations of WD 1418–088. The dotted line marks the weighted mean of the velocity measurements.

Bédard et al. (2017) showed that there is a significant discrepancy between the spectroscopic and photometric solutions for WD 1418–088. Under the assumption of a single star, the spectroscopic fits (corrected for 3D effects) indicate $T_{\rm eff} = 8060$ K, $\log g = 8.1$, and $M = 0.66 \, M_{\odot}$, whereas the photometric fits using the *Gaia* DR2 parallax measurement indicate much lower $\log g = 7.55$ and $M = 0.36 \, M_{\odot}$ (Blouin et al. 2019). The only way to resolve the discrepancy between the photometric and spectroscopic solutions is if WD 1418–088 is a binary system. The combined light from the two stars in an unresolved binary would make it appear more luminous, which could be interpreted as a single white dwarf having a larger radius, and therefore a lower mass.

Given the limited number of radial velocity observations over monthly and yearly time-scales, our observations of WD 1418–088 are not sensitive to long-period systems. To estimate the detection efficiency of a binary system as a function of orbital period, we use a Monte Carlo approach, and generate synthetic radial velocity measurements with the same temporal sampling and accuracy as the WD 1418–088 observations. We assume a mass ratio of one, and include the projection effects due to
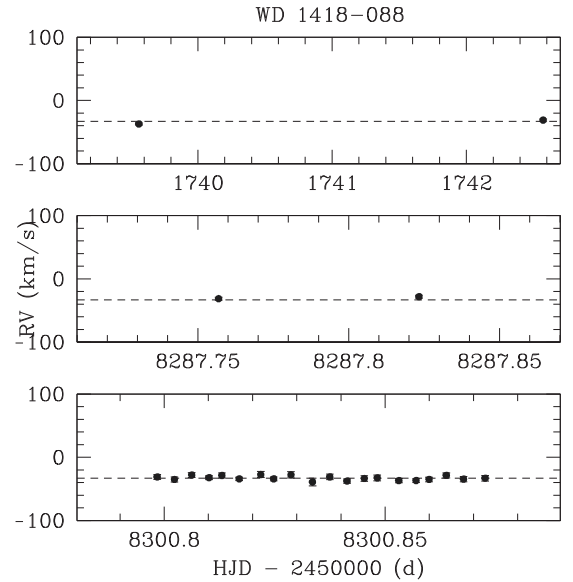
randomly oriented orbits. We estimate our detection efficiency using the number of trials, which satisfy the detection criterion of $\log (p) < -4$ (see Maxted et al. 2000). Fig. 7 shows the detection efficiency of our observations for WD 1418–088 for orbital periods ranging from 1 to 1000 d. This figure shows that we would have detected the majority of the binary systems with orbital periods ≤70 d, but our detection efficiency significantly deteriorates beyond 80 d. Hence, WD 1418–088 is likely a long-period binary white dwarf system. One of the overluminous white dwarfs included in the Bédard et al. (2017) study, WD 1639+153, is an astrometric binary with an orbital period of 4 yr. Hence, WD 1418–088 may be an unresolved binary with a similarly long orbital period.
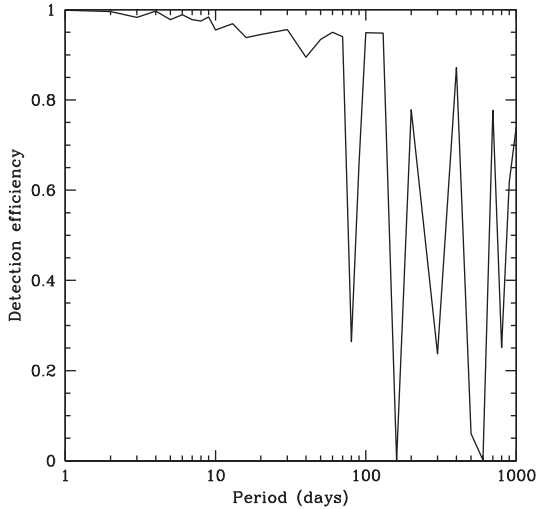
Figure 7. The detection efficiency as a function of orbital period for WD 1418–088, assuming an equal-mass binary system.

Fig. 8 displays our best model-atmosphere fit to the spectroscopic and photometric observations of WD 1418–088 (as well as WD 1447–190 and WD 1606+422) assuming a DA+DA binary system. Here, in the absence of an orbital solution, all four atmospheric parameters are allowed to vary in the fitting procedure and are thus less tightly constrained than those in the case of WD 0311–649. We derive $T_{\mathrm{eff},1} = 8500 \pm 1000$ K, $\log g_1 = 8.00 \pm 0.20$ and $T_{\mathrm{eff},2} = 6100 \pm 500$ K, $\log g_2 = 8.15 \pm 0.20$, which correspond to $M_1 = 0.60^{+0.12}_{-0.11}$ M$_\odot$ and $M_2 = 0.68^{+0.13}_{-0.12}$ M$_\odot$ according to the mass–radius relation. The agreement between the data and the model is excellent, but the errors in our surface gravity and mass estimates are relatively large due to the lack of any orbital constraints in this system. The best-fitting model indicates a visible/near-infrared flux ratio of ∼2–5 between the primary and secondary stars. If this is a long-period binary, high-resolution imaging observations may be able to resolve it (e.g. Harris et al. 2013).

Andrews, Breivik & Chatterjee (2019) demonstrate that *Gaia* astrometry can find hidden white dwarf companions at distances as far as several hundred parsec. In addition, *Gaia* can characterize orbits with periods ranging from 10 d to thousands of days. Using 0.1 mas as the size of the primary star's orbit resolvable by *Gaia* (Andrews et al. 2019) and a distance of 37 pc, *Gaia* should be able to easily resolve the astrometric orbit for WD 1418–088 within the next several years.

5.3 WD 1447–190

Fig. 9 shows the radial velocity measurements and the Lomb–Scargle periodogram for the single-lined binary WD 1447–190. There are no significant period aliases in the Lomb–Scargle diagram. We perform 1000 Monte Carlo simulations for our orbital fits, and the results are consistent with the formal estimates from MPRV-FIT. The best-fitting orbital solution has $P = 1.790\,83 \pm 0.000\,04$ d, $K = 83.8^{+1.2}_{-1.3}$ km s^{-1}, $\gamma = -32.7^{+0.8}_{-0.9}$ km s^{-1}, and a mass function of $f = 0.109 \pm 0.005$ M$_\odot$.

Our best model-atmosphere fit to the Balmer lines and energy distribution of WD 1447–190 is presented in Fig. 8. Given the lack of a complete orbital solution, all four atmospheric parameters are considered as free parameters in the minimization process. We find $T_{\mathrm{eff},1} = 8000 \pm 1000$ K, $\log g_1 = 7.65 \pm 0.20$ and $T_{\mathrm{eff},2} =$

5000 $\pm$ 500 K, $\log g_2 = 7.50 \pm 0.20$, which convert to $M_1 = 0.41^{+0.10}_{-0.08}$ M$_\odot$ and $M_2 = 0.33^{+0.09}_{-0.07}$ M$_\odot$ using our evolutionary sequences. Again, our composite model reproduces the spectroscopy and photometry relatively well. For $M_1 = 0.41$ M$_\odot$, the mass function requires $M_2 \geq 0.42$ M$_\odot$, which suggests that the secondary mass is closer to the upper limit of the mass range indicated by our model atmosphere analysis. Interestingly, our solution provides an elegant explanation for the single-lined nature of this binary system: The secondary white dwarf has a very low effective temperature; hence, its Hα feature is simply too weak to be observed.

5.4 WD 1606+422

Fig. 10 shows the radial velocity measurements and the Lomb–Scargle periodogram for the double-lined spectroscopic binary WD 1606+422. Excluding the two spectra where the Hα lines from both stars overlap and appear as a single line, we have 40 velocity measurements for each star. The best-fitting orbital solution has $P = 0.839\,35 \pm 0.000\,02$ d, $K_1 = 123.0 \pm 1.7$ km s^{-1}, $K_2 = 92.7 \pm 1.5$ km s^{-1}, $\gamma_1 = -33.6 \pm 1.5$ km s^{-1}, and a velocity offset of $\gamma_2 - \gamma_1 = 13.4 \pm 2.5$ km s^{-1}.

The Lomb–Scargle periodogram shows that the period is well constrained for WD 1606+422. Performing 1000 Monte Carlo simulations, we derive $P = 0.839\,35 \pm 0.000\,02$ d, $K_1 = 123.0^{+1.7}_{-1.8}$ km s^{-1}, $K_2 = 92.8 \pm 1.7$ km s^{-1}, $\gamma_1 = -33.4^{+1.8}_{-1.9}$ km s^{-1}, $\gamma_2 - \gamma_1 = 13.0^{+3.0}_{-3.2}$ km s^{-1}, and $\frac{K_1}{K_2} = 1.33 \pm 0.03$.

Following our usual procedure, we find that there exists no solution satisfying all available constraints (orbital parameters, spectroscopy, and photometry) simultaneously. However, a consistent solution is achievable if the velocity offset is slightly smaller. Therefore, in what follows, we adopt $\gamma_2 - \gamma_1 = 11.0$ km s^{-1}, but keep the original confidence interval for the error propagation. Solving equation (2) then yields $M_1 = 0.445^{+0.103}_{-0.039}$ M$_\odot$ and $M_2 = 0.592^{+0.124}_{-0.045}$ M$_\odot$.

Fig. 8 displays our best model-atmosphere fit to the spectroscopic and photometric data of WD 1606+422. As in the case of the other double-lined system WD 0311–649, we assume the surface gravities corresponding to the masses derived from the orbital parameters, $\log g_1 = 7.70^{+0.19}_{-0.09}$ and $\log g_2 = 7.97^{+0.19}_{-0.08}$, while the effective temperatures are determined from the fit. We obtain $T_{\mathrm{eff},1} = 11\,500 \pm 500$ K and $T_{\mathrm{eff},2} = 13\,300 \pm 500$ K, for which the Balmer lines and the spectral energy distribution are reproduced well.

Fig. 11 compares the observed double Hα feature of WD 1606+422 with that predicted by our best-fitting solution. As before, we improve the signal-to-noise by co-adding five of our Gemini spectra, and we shift the individual synthetic spectra so that the positions of the observed and theoretical line cores coincide. The agreement is quite good, although our model spectra appear slightly too shallow in the very core of the lines. Finally, similar to WD 0311–649, our analysis suggests that the cooler white dwarf in WD 1606+422 falls within the ZZ Ceti instability strip (Gianninas et al. 2011). Interestingly enough, Gianninas et al. (2011) and Bognár et al. (2018) reported WD 1606+422 to be photometrically constant. However, it is possible that the luminosity variations have not been detected yet because of their dilution by the light of the hotter component. Thus, we recommend that WD 1606+422 be further monitored for photometric variability.

6 DISCUSSION

Bédard et al. (2017) identified 15 overluminous white dwarfs in their parallax sample that are inconsistent with being single white dwarfs.
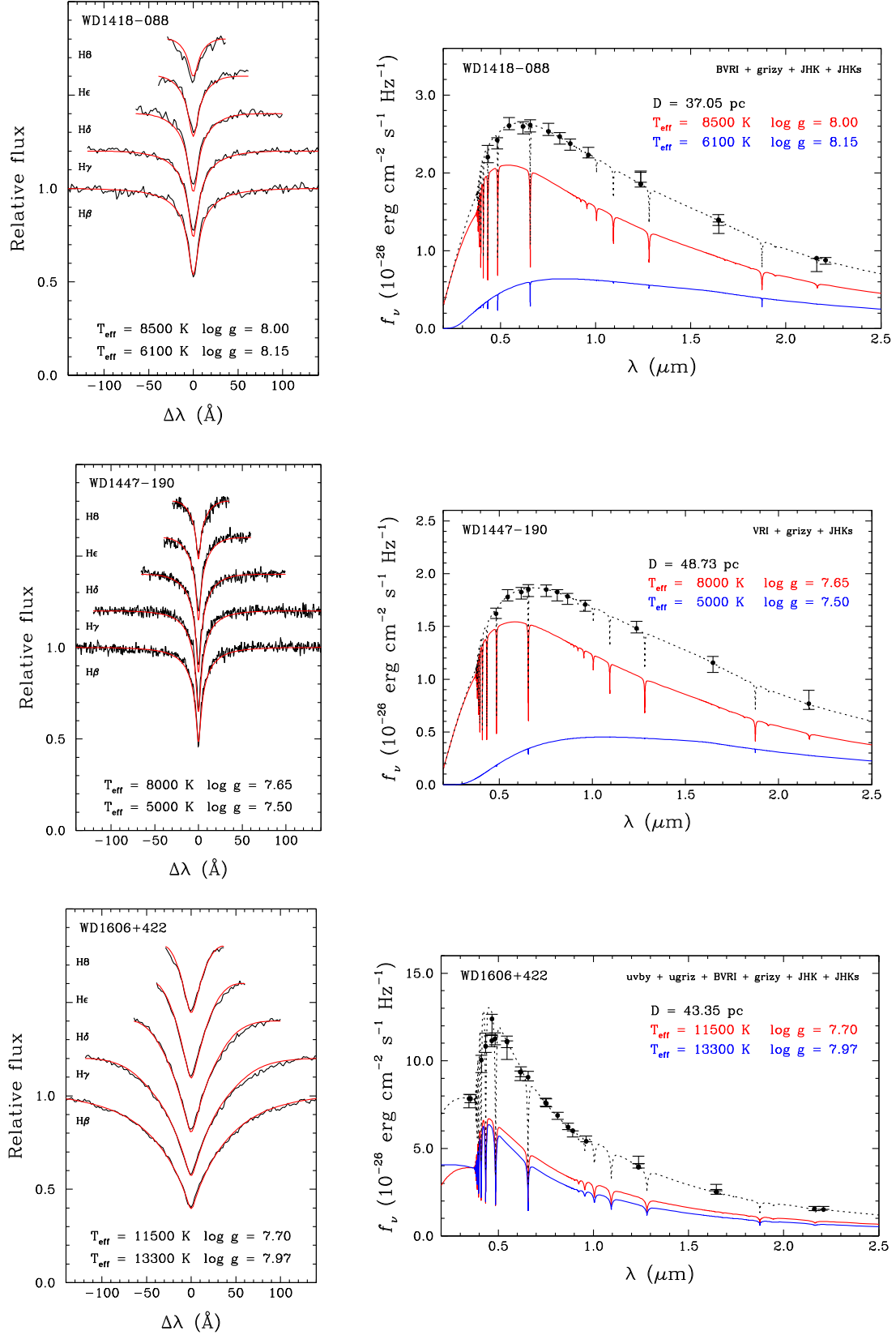
Figure 8. Same as Fig. 4, but for WD 1418–088, WD 1447–190, and WD 1606+422.
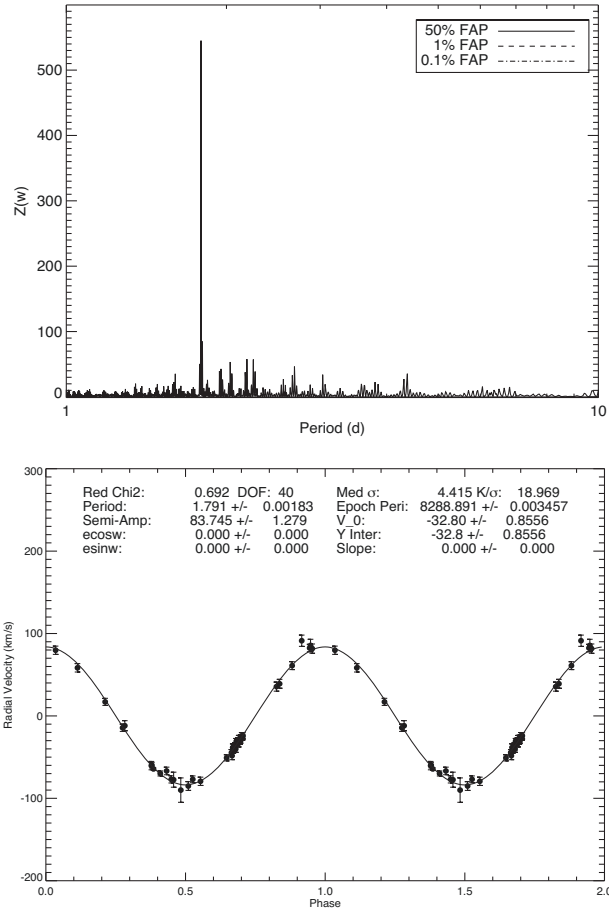
Figure 9. *Top:* Lomb–Scargle periodogram for WD 1447–190. The period is well constrained and there are no significant period aliases. *Bottom:* Radial velocity measurements and the best-fitting orbital solution (solid line) for WD 1447–190 assuming a circular orbit. The best-fitting orbital period is 1.79 d.

Gaia DR2 parallaxes confirm the overluminous nature of all but one of these targets, WD 1130+189. Out of the 14 remaining binary candidates, one (WD 2048+809) lacks follow-up spectroscopy, four are SB2, four are SB1, and one is a long-period astrometric binary.

Table 1 presents the orbital parameters of all nine confirmed binary systems in this sample. The four SB2 systems have periods ranging from 0.12 to 1.56 d with mass ratios of 1.1–1.4, whereas the four SB1 systems have periods in the range ∼1–6 d. The newly identified double-lined system WD 0311–649 is almost a twin of the WD 1242–105 binary, though with a much longer orbital period (0.74 d versus 0.12 d). WD 1639+153 is a $P = 4$ yr astrometric binary detected in ground-based parallax observations by Harris et al. (2013). Such long-period binary systems are extremely difficult to confirm by radial velocity observations, and are likely hiding in overluminous white dwarf samples.

Four of the targets in our sample have follow-up radial velocity observations, which effectively rule out short-period binary systems. In addition to WD 1418–088 discussed above, WD0126+101, WD0142+312, and WD2111+261 (Maxted et al. 2000; Napiwotzki et al. 2019) have 8–12 radial velocity observations that do not reveal any significant variability. However, all of these targets appear overluminous based on their parallax measurements. In addition, atmospheric model fits to their spectra suggest average-
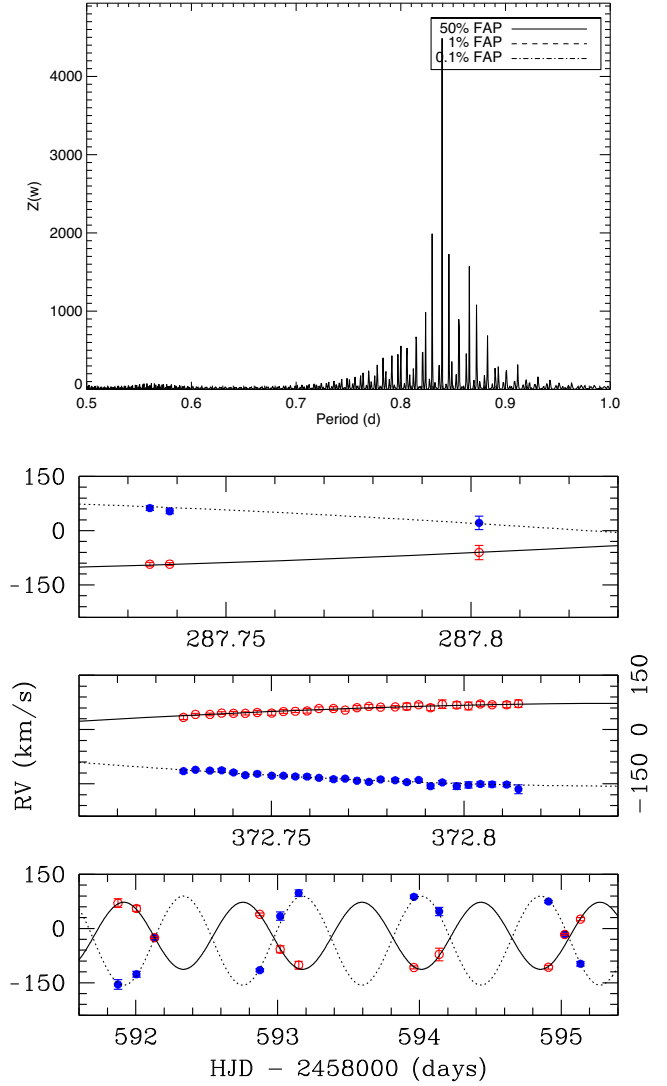

Figure 10. *Top:* Lomb–Scargle periodogram for WD 1606+422. *Bottom:* Radial velocity measurements (open and filled points) and the best-fitting orbital solutions (dotted and solid lines) for the two stars in WD 1606+422 assuming a circular orbit.
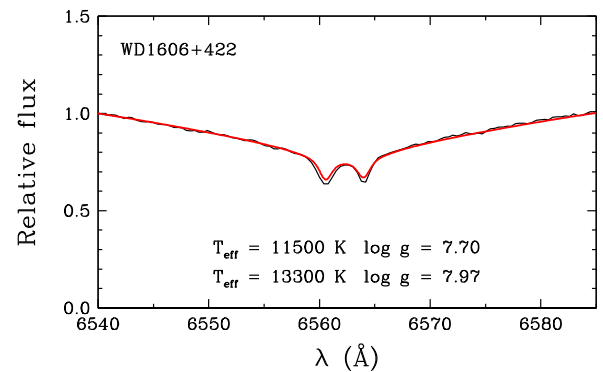

Figure 11. Comparison of the observed double Hα feature of WD 1606+422, shown as the black line, with that predicted by our best model-atmosphere fit, displayed as the red line.
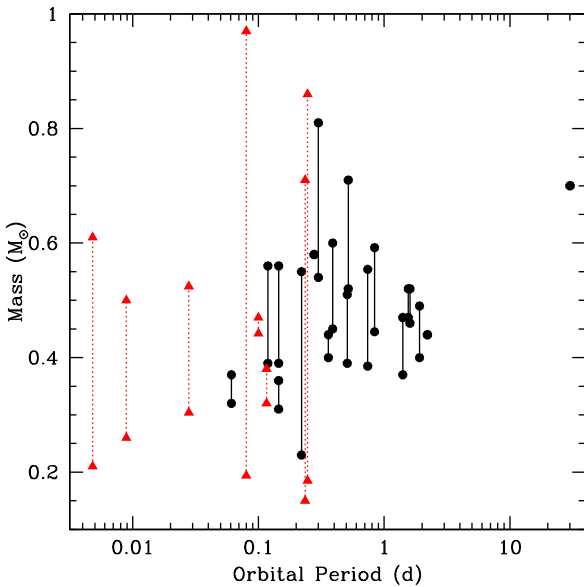
Figure 12. Mass and orbital period distribution of all known SB2 (circles) and eclipsing (triangles) double white dwarfs with orbital constraints. The lines connect the components of each binary.

mass white dwarfs, whereas fits to their photometry indicate much lower masses.

For example, WD 0142+312 has the best-fitting spectroscopic estimates of $T_{eff} = 9270 \pm 130$ K and $\log g = 8.12 \pm 0.05$ (Limoges, Bergeron & Lépine [2015]), whereas the photometric fit indicates $T_{eff} = 8790$ K and $\log g = 7.54$. Both WD 0142+312 and WD 2111+261 are inconsistent with being single stars at the $>5\sigma$ level. The case for a binary system is weaker for WD 0126+101, as the best-fitting estimates from spectroscopy and photometry differ by only 2σ. Nevertheless, it is clear that at least three (WD 0142+312, WD 1418−088, and WD 2111+261), and perhaps all four of these objects without any significant radial velocity variations must be binary white dwarfs.

Our observations, as well as the previous radial velocity measurements in the literature, of these targets are not sensitive to month- and year-long orbital periods, and would not be able to detect long-period systems like the astrometric binary WD 1639+153 (Harris et al. [2013]). Hence, these four targets are likely long-period binary systems that can be confirmed through either high-resolution imaging observations or *Gaia* astrometry (Andrews et al. [2019]).

It is interesting to compare our binary sample to that of the larger sample from the SPY survey. Napiwotzki et al. ([2019]) identified 39 double-degenerate binaries, half of which are SB2 systems. However, they found significant radial velocity variations in only 16 of the 44 low-mass ($M \leq 0.45\,M_{\odot}$) white dwarfs in their sample, indicating that either these low-mass white dwarfs are single or that they have substellar mass companions. Given that the mean detection efficiency of the SPY survey degrades quickly for month and longer time-scales (Napiwotzki et al. [2019]; see their fig. 6), it is likely that a significant fraction of these are long-period binary white dwarfs with higher masses. For example, two of the overluminous white dwarfs in the Bédard et al. ([2017]) sample, WD 0126+101 and WD 1418−088, are included in the SPY sample as single low-mass white dwarfs, but our analysis suggests that they are instead long-period binary systems of more massive white dwarfs.

Fig. [12] shows the mass and orbital period distribution of all known double-lined spectroscopic binary white dwarfs and eclips-

ing double white dwarfs. The lines connect the components of each binary. We limit this figure to only SB2 and eclipsing systems, where the component masses can be constrained reliably. There are 19 SB2 white dwarfs, including the two newly identified systems presented in this work, and 8 eclipsing systems (Hallakoun et al. [2016]; Burdge et al. [2019], and references therein). The latter are found at short orbital periods ($P \leq 0.25$ d), and dominated by ELM white dwarfs, which usually have relatively massive companions (Andrews et al. [2014]; Boffin [2015]; Brown et al. [2017]). On the other hand, the double-lined binaries are nearly equal-mass ratio systems. This is not surprising as the spectral lines from both stars would be visible only if both have comparable luminosities, which depend on the radii, and therefore the masses of the two white dwarfs in the system. With further discoveries of double-lined systems among the overluminous white dwarf population in *Gaia* (Marsh [2019]), we may finally be able to have a large enough sample of SB2 systems to compare against and constrain the population synthesis models for double white dwarfs (e.g. Nelemans et al. [2001]).

7 CONCLUSIONS

We presented follow-up spectroscopy of four overluminous white dwarfs identified by Bédard et al. ([2017]). Two of these, WD 0311−649 and WD 1606+422, are double-lined systems, and we provide orbital periods, mass ratios, component masses, and effective temperatures of each binary based on their spectral line profiles, spectral energy distributions, and radial velocity data. An additional system, WD 1447−190, is a single-lined binary with a period of 1.79 d, whereas WD 1418−088 does not show any significant velocity variations.

Studying the 15 overluminous white dwarfs in the Bédard et al. ([2017]) sample, and ignoring WD 2048+809 (no follow-up spectroscopy) and WD 1130+189 (not overluminous based on *Gaia* DR2 parallax), we find that four are SB2, four are SB1, one is an astrometric binary, and four appear to show no significant radial velocity variations. However, there are significant discrepancies between the spectroscopic and photometric fits for the latter four stars, and the only way to resolve this issue is if they are in long-period binary systems. Follow-up high-spatial resolution imaging and/or *Gaia* astrometry (Andrews et al. [2019]) may resolve these four systems. We also argue that the overabundance of single low-mass white dwarfs in the SPY survey (Napiwotzki et al. [2019]) is likely due to a similar problem, and that at least some of those objects are likely in long-period binary systems as well.

Our results provide strong evidence that all 13 of these overluminous white dwarfs with follow-up spectroscopy are indeed double degenerates. In addition, one of these systems, WD 1242−105, has a short enough orbital period to merge within a Hubble time (Debes et al. [2015]). However, we refrain from discussing the implications of our results on the overall space density and merger rate of double white dwarfs due to biases in our sample selection. The 219 stars analysed in Bédard et al. ([2017]) were selected simply because they had a parallax measurement available at the time. They also used parallax measurements from several different sources (e.g. *Hipparcos*, Yale Parallax Catalog, USNO, and *Gaia* DR1). Hence, our overluminous white dwarf sample has strong selection effects and is not statistically complete.

REFERENCES

Andrews J. J., Price-Whelan A. M., Agüeros M. A., 2014, ApJ, 797, L32
Andrews J. J., Breivik K., Chatterjee S., 2019, ApJ, 886, 68
Bédard A., Bergeron P., Fontaine G., 2017, ApJ, 848, 11
Bergeron P., Dufour P., Fontaine G., Coutu S., Blouin S., Genest-Beaulieu C., Bédard A., Rolland B., 2019, ApJ, 876, 67
Blouin S., Dufour P., Thibeault C., Allard N. F., 2019, ApJ, 878, 63
Boffin H. M. J., 2015, A&A, 575, L13
Bognár Z., Kalup C., Sódor Á., Charpinet S., Hermes J. J., 2018, MNRAS, 478, 2676
Bours M. C. P. et al., 2014, MNRAS, 438, 3399
Brown W. R., Kilic M., Hermes J. J., Allende Prieto C., Kenyon S. J., Winget D. E., 2011, ApJ, 737, L23
Brown W. R., Gianninas A., Kilic M., Kenyon S. J., Allende Prieto C., 2016, ApJ, 818, 155
Brown W. R., Kilic M., Kosakowski A., Gianninas A., 2017, ApJ, 847, 10
Burdge K. B. et al., 2019, Nature, 571, 528
Chambers K. C. et al., 2016, preprint (arXiv:1612.05560)
Clemens J. C., Crain J. A., Anderson R., 2004, in Alan F. M. M., Masanori I., eds, Proc. SPIE Conf. Ser. Vol. 5492, Ground-Based Instrumentation for Astronomy. SPIE, Bellingham, p. 331
Debes J. H., Kilic M., Tremblay P.-E., López-Morales M., Anglada-Escude G., Napiwotzki R., Osip D., Weinberger A., 2015, AJ, 149, 176
De Lee N. et al., 2013, AJ, 145, 155
Fontaine G., Brassard P., Bergeron P., 2001, PASP, 113, 409
Gaia Collaboration, 2018, A&A, 616, A1
Gianninas A., Bergeron P., Ruiz M. T., 2011, ApJ, 743, 138
Hallakoun N. et al., 2016, MNRAS, 458, 845

Harris H. C. et al., 2013, ApJ, 779, 21
Holberg J. B., Bergeron P., 2006, AJ, 132, 1221
Karl C. A., Napiwotzki R., Nelemans G., Christlieb N., Koester D., Heber U., Reimers D., 2003, A&A, 410, 663
Li Z., Chen X., Chen H.-L., Han Z., 2019, ApJ, 871, 148
Limoges M.-M., Bergeron P., Lépine S., 2015, ApJS, 219, 19
Marsh T. R., 1995, MNRAS, 275, L1
Marsh T. R., 2019, Close Double White Dwarfs in Gaia, DOI 10.5281/zenodo.3265937
Maxted P. F. L., Ferrario L., Marsh T. R., Wickramasinghe D. T., 2000, MNRAS, 315, L41
Maxted P. F. L., Marsh T. R., Moran C. K. J., 2002, MNRAS, 332, 745
Morales-Rueda L., Marsh T. R., Maxted P. F. L., Nelemans G., Karl C., Napiwotzki R., Moran C. K. J., 2005, MNRAS, 359, 648
Moran C., Marsh T. R., Bragaglia A., 1997, MNRAS, 288, 538
Napiwotzki R. et al., 2001, Astron. Nachr., 322, 411
Napiwotzki R. et al., 2002, A&A, 386, 957
Napiwotzki R. et al., 2007, in Ralf N., Matthew R. B., eds, ASP Conf. Ser. Vol. 372, 15th European Workshop on White Dwarfs. Astron. Soc. Pac., San Francisco, p. 387
Napiwotzki R. et al., 2019, A&A, preprint (arXiv:1906.10977)
Nelemans G., Yungelson L. R., Portegies Zwart S. F., Verbunt F., 2001, A&A, 365, 491
Nelemans G. et al., 2005, A&A, 440, 1087
Newville M., Stensitzki T., Allen D. B., Ingargiola A., 2014, zndo, doi:10.5281/zenodo.11813
Rebassa-Mansergas A., Parsons S. G., García-Berro E., Gänsicke B. T., Schreiber M. R., Rybicka M., Koester D., 2017, MNRAS, 466, 1575
Saffer R. A., Liebert J., Olszewski E. W., 1988, ApJ, 334, 947
Steinfadt J. D. R., Kaplan D. L., Shporer A., Bildsten L., Howell S. B., 2010, ApJ, 716, L146
Subasavage J. P. et al., 2017, AJ, 154, 32
Tremblay P.-E., Bergeron P., 2009, ApJ, 696, 1755
Tremblay P.-E., Ludwig H.-G., Steffen M., Freytag B., 2013, A&A, 559, A104
Vogt S. S. et al., 1994, in David L. C., Eric R. C., eds, Proc. SPIE Conf. Ser. Vol. 2198, Instrumentation in Astronomy VIII. SPIE, Bellingham, p. 362

APPENDIX A: RADIAL VELOCITY DATA

Table A1. WD 0311–649.

HJD−2450000 (days)	$V1_{helio}$ (km s^{-1})	$V2_{helio}$ (km s^{-1})
8393.74603027	0.0 ± 3.9	133.7 ± 4.0
8393.74800758	− 5.3 ± 7.3	134.8 ± 4.8
8393.75141472	− 4.2 ± 6.2	137.1 ± 5.4
8393.75339236	3.5 ± 10.2	133.4 ± 5.7
8393.75536627	0.2 ± 7.7	141.4 ± 6.4
8393.75734092	1.3 ± 7.2	138.3 ± 5.5
8393.75931542	5.6 ± 11.3	135.8 ± 9.5
8393.76129677	8.9 ± 8.2	138.1 ± 5.3
8393.76326492	3.3 ± 7.4	131.4 ± 5.3
8393.76619544	− 2.6 ± 7.9	133.0 ± 5.3
8393.76817239	7.2 ± 5.7	135.1 ± 4.3
8393.77014865	5.2 ± 8.1	134.0 ± 6.2
8393.77213876	1.6 ± 8.7	140.4 ± 7.5
8393.77411675	11.0 ± 10.5	140.1 ± 7.2
8393.77608770	− 0.7 ± 8.9	125.3 ± 7.9
8393.77806197	− 3.5 ± 4.9	128.8 ± 5.0
8393.78099341	− 4.8 ± 6.6	129.4 ± 4.9
8393.78297661	3.4 ± 7.0	136.4 ± 4.9
8393.78494521	5.5 ± 7.7	128.0 ± 5.5
8393.78691986	10.0 ± 7.1	133.4 ± 4.8

Table A1 – *continued*

HJD−2450000 (days)	$V1_{\rm helio}$ (km s^{-1})	$V2_{\rm helio}$ (km s^{-1})
8393.78889460	4.2 ± 10.9	127.6 ± 5.1
8393.79087339	3.6 ± 8.2	130.9 ± 6.1
8393.79284709	10.1 ± 5.4	128.8 ± 3.9
8393.79576315	0.4 ± 6.8	130.4 ± 5.8
8393.79773732	14.9 ± 12.8	131.9 ± 8.3
8393.79971394	13.0 ± 6.1	132.4 ± 4.4
8393.80169190	3.7 ± 8.8	127.9 ± 4.9
8393.80366792	4.5 ± 7.7	123.9 ± 5.2
8393.80564173	7.6 ± 5.6	120.7 ± 4.8
8393.80761778	18.7 ± 10.3	132.2 ± 5.3
8393.81101586	12.4 ± 6.4	122.1 ± 5.3
8393.81299096	8.3 ± 11.5	122.5 ± 8.8
8393.81496490	14.1 ± 8.5	122.5 ± 9.6
8393.81694324	− 0.9 ± 9.2	117.8 ± 7.3
8393.81891741	0.4 ± 8.9	117.4 ± 6.2
8393.82089272	4.8 ± 10.8	115.2 ± 7.2
8393.82286781	13.7 ± 10.0	117.3 ± 8.3
8393.82578447	3.3 ± 9.8	118.3 ± 6.0
8393.82775933	5.8 ± 6.3	119.1 ± 7.5
8393.82973347	9.7 ± 8.5	116.8 ± 7.3
8393.83172374	12.0 ± 11.7	111.9 ± 7.1
8393.83369756	10.7 ± 11.1	104.8 ± 5.7
8393.83568803	16.5 ± 8.7	108.8 ± 7.1
8393.83767901	− 1.0 ± 21.2	97.1 ± 9.7
8393.84061334	11.5 ± 17.6	106.2 ± 12.2
8393.84258957	15.3 ± 7.9	103.6 ± 7.0
8393.84456527	23.9 ± 11.4	106.5 ± 11.1
8393.84655678	16.4 ± 20.3	101.5 ± 12.2
8393.84853167	11.4 ± 12.6	97.4 ± 8.5
8393.85050650	22.0 ± 8.5	99.2 ± 11.6
8393.85248162	21.3 ± 12.4	105.2 ± 13.2
8393.85540216	5.2 ± 25.6	92.3 ± 15.2
8393.85737970	16.2 ± 29.0	88.6 ± 19.3
8393.85936985	25.3 ± 12.3	99.8 ± 11.3
8393.86134366	11.2 ± 12.6	84.8 ± 9.8
8393.86333390	24.7 ± 13.2	93.8 ± 8.9
8393.86532509	25.3 ± 13.5	95.5 ± 12.4
8796.50239379	114.0 ± 7.1	− 24.3 ± 7.5
8796.64593769	56.3 ± 5.5	56.3 ± 5.5
8796.79867849	3.3 ± 9.7	127.6 ± 7.9
8797.57631070	14.1 ± 9.5	131.7 ± 8.0
8797.67691008	56.1 ± 15.0	97.2 ± 10.5

Table A1 – *continued*

HJD−2450000 (days)	$V1_{\rm helio}$ (km s^{-1})	$V2_{\rm helio}$ (km s^{-1})
8797.86212509	116.4 ± 6.6	− 25.8 ± 4.3
8798.51407694	57.5 ± 11.4	11.7 ± 7.6
8798.70385557	117.1 ± 8.2	− 28.2 ± 6.4
8798.81964492	46.5 ± 3.4	46.5 ± 3.4
8799.51585147	96.1 ± 12.8	− 3.3 ± 13.1
8799.75808955	1.7 ± 7.7	129.0 ± 5.8
8799.76176339	− 1.8 ± 10.0	135.1 ± 8.5
8801.51700741	103.5 ± 12.3	− 10.6 ± 9.3
8801.79271799	51.0 ± 2.2	51.0 ± 2.2

Table A2. WD 1418–088.

HJD−2450000 (days)	$V_{\rm helio}$ (km s^{-1})
1739.5605	−37.1 ± 1.5
1742.5722	−30.9 ± 1.6
8287.75722641	−31.3 ± 2.3
8287.82388136	−28.2 ± 2.4
8300.79887603	−31.1 ± 3.9
8300.80257108	−35.1 ± 4.1
8300.80700933	−28.2 ± 3.7
8300.81070462	−32.3 ± 3.1
8300.81440187	−28.8 ± 4.0
8300.81809752	−34.2 ± 2.6
8300.82252975	−27.2 ± 4.8
8300.82622664	−34.2 ± 3.1
8300.82992265	−27.7 ± 4.8
8300.83361871	−39.1 ± 6.0
8300.83829250	−31.1 ± 4.4
8300.84198874	−37.6 ± 3.4
8300.84568688	−33.6 ± 4.2
8300.84938494	−32.6 ± 4.6
8300.85382737	−36.8 ± 3.4
8300.85752113	−36.8 ± 3.0
8300.86121842	−35.1 ± 3.5
8300.86491463	−28.6 ± 3.9
8300.86934108	−34.6 ± 4.3
8300.87303809	−33.2 ± 4.3

Table A3. WD 1447−190.

HJD−2450000 (days)	V_{helio} (km s^{-1})
8287.79004386	− 97.1 ± 1.5
8287.83398725	− 102.6 ± 3.1
8309.78038901	− 77.4 ± 3.8
8309.78408475	− 81.1 ± 4.8
8309.78851329	− 71.1 ± 4.4
8309.79220918	− 74.4 ± 3.9
8309.79590724	− 71.6 ± 4.6
8309.79960426	− 69.4 ± 2.6
8309.80402782	− 70.0 ± 4.9
8309.80771825	− 72.9 ± 4.1
8309.81141411	− 63.6 ± 3.4
8309.81511482	− 66.0 ± 4.0
8309.81953192	− 65.9 ± 3.2
8309.82322608	− 63.0 ± 3.8
8309.82692321	− 63.5 ± 7.0
8309.83062011	− 60.4 ± 4.0
8309.83504889	− 63.4 ± 3.7
8309.83874442	− 62.9 ± 2.9
8309.84244060	− 58.3 ± 2.8
8309.84613589	− 57.4 ± 4.5
8309.85055716	− 58.7 ± 3.8
8309.85425293	− 57.0 ± 3.8
8544.82924001	58.4 ± 6.8
8544.88585415	52.7 ± 7.5
8545.75376632	− 99.6 ± 4.6
8545.79880531	− 110.2 ± 9.1
8545.84483738	− 122.8 ± 14.8
8545.89278086	− 117.9 ± 5.3
8546.83294299	46.9 ± 5.0
8588.63922836	− 92.5 ± 3.4
8588.76353703	− 109.8 ± 4.4
8588.90132700	− 109.7 ± 4.1
8602.77792314	− 47.2 ± 4.4
8602.79230148	− 44.7 ± 6.1
8603.86506466	28.2 ± 4.8
8605.55550400	2.8 ± 5.5
8605.76824108	49.6 ± 4.5
8606.54405099	− 93.1 ± 5.1
8606.85924347	− 112.1 ± 5.0
8616.52990044	48.9 ± 5.6
8616.81562358	25.6 ± 5.1
8636.69212753	− 15.7 ± 4.3
8637.47080183	− 83.7 ± 3.7
8637.81049184	6.2 ± 5.4

Table A4. WD 1606+422.

HJD−2450000 (days)	$V1_{helio}$ (km s^{-1})	$V2_{helio}$ (km s^{-1})
8287.73442998	62.1 ± 6.7	− 92.9 ± 5.4
8287.73849062	53.7 ± 6.7	− 92.6 ± 4.2
8287.80162519	21.6 ± 18.4	− 60.4 ± 19.5
8372.72714356	− 115.1 ± 4.9	33.9 ± 6.0
8372.73020305	− 111.2 ± 3.0	41.7 ± 2.9
8372.73398796	− 113.2 ± 3.1	41.8 ± 3.8
8372.73704803	− 112.7 ± 5.2	45.7 ± 3.8
8372.74011007	− 118.4 ± 4.4	45.0 ± 4.8
8372.74316907	− 126.0 ± 3.0	45.1 ± 4.4
8372.74623077	− 122.7 ± 5.1	47.3 ± 5.7
8372.75003536	− 127.5 ± 4.0	45.6 ± 5.9
8372.75309717	− 127.8 ± 3.2	49.8 ± 5.1
8372.75615667	− 129.7 ± 4.0	50.4 ± 3.3
8372.75921767	− 130.2 ± 4.7	51.7 ± 6.4
8372.76227795	− 133.7 ± 3.4	58.4 ± 4.1
8372.76606043	− 137.4 ± 5.0	58.2 ± 4.9
8372.76911994	− 136.0 ± 4.3	54.0 ± 3.3
8372.77217918	− 141.4 ± 3.1	60.3 ± 6.1
8372.77524041	− 144.9 ± 3.5	64.0 ± 5.0
8372.77830567	− 138.1 ± 4.2	62.2 ± 3.6
8372.78208815	− 140.1 ± 4.7	62.7 ± 3.9
8372.78514742	− 145.3 ± 3.9	63.9 ± 9.5
8372.78820890	− 139.6 ± 3.3	68.4 ± 5.2
8372.79126849	− 156.7 ± 6.3	60.3 ± 8.1
8372.79432937	− 146.1 ± 5.0	70.0 ± 11.8
8372.79810607	− 156.5 ± 8.6	67.9 ± 8.6
8372.80116626	− 153.1 ± 8.8	65.3 ± 10.6
8372.80422631	− 150.8 ± 5.8	70.7 ± 6.6
8372.80728686	− 151.7 ± 7.0	68.7 ± 5.3
8372.81106865	− 152.2 ± 6.1	68.7 ± 7.9
8372.81412870	− 165.0 ± 11.9	71.5 ± 10.6
8591.87407156	− 154.6 ± 13.5	70.2 ± 12.0
8592.00464574	− 126.5 ± 8.1	55.2 ± 7.8
8592.13206901	− 25.2 ± 2.8	− 25.2 ± 2.8
8592.87443003	− 115.1 ± 3.9	39.0 ± 3.5
8593.01822250	34.1 ± 11.5	− 57.6 ± 9.6
8593.14855262	97.7 ± 8.9	− 101.3 ± 10.8
8593.96107311	87.5 ± 4.8	− 107.7 ± 4.2
8594.13898214	47.1 ± 11.7	− 71.8 ± 17.4
8594.90966600	74.8 ± 3.3	− 107.2 ± 5.3
8595.02447094	− 16.3 ± 2.4	− 16.3 ± 2.4
8595.13547162	− 97.8 ± 6.4	25.7 ± 4.6

This paper has been typeset from a TEX/LATEX file prepared by the author.